Design and Verification of 150-krpm PMSM Based on Experiment Results of Prototype

Myung-Seop Lim, Seung-Hee Chai, Jae-Sik Yang, and Jung-Pyo Hong, *Senior Member, IEEE*

***Abstract*—This paper proposes the design process of a 2.62-kW 150-krpm high-speed surface-mounted permanent-magnet synchronous motor. To meet the required specifications, the numbers of poles and slots were determined by considering the maximum speed and the rotary stability affected by the vibration of the rotor. In addition, this paper describes not only the appropriate material selection method but also the appropriate geometry design method based on analytic approaches. Furthermore, to precisely evaluate the bearing and windage losses at a high speed, a method that combines the finite-element method and the experiment results of the prototype was used. As a result, an improved motor was designed, which had higher maximum power and speed than the prototype and a lower mass moment of inertia. Finally, tests were conducted to verify the validity of the proposed design process and the effectiveness of the motor.**

***Index Terms*—Copper loss, eddy current loss, high-speed machine, iron loss, mechanical loss, surface-mounted permanent-magnet synchronous motor (SPMSM), vibration.**

I. Introduction

THE RISING demand for high-speed machines in various industry applications, such as direct-drive generators, air blowers, and machining spindles, has led to intensive research on the design method for such machines. Using high-speed motors instead of geared standard motors increases system reliability and offers the opportunity to reduce cost. The main benefits of gearless directly coupled high-speed machines are the elimination of the gear costs and the prevention of oil leakage and maintenance and gear losses. Noise can also be significantly reduced as there is no need for an additional transmission system. While high-speed machines achieve high power from their high rotational speed and small torque, small and compact motors allow for new integrated system construction [1].

For the aforementioned applications, permanent magnet (PM) machines are recognized as favorites due to their high power densities and relatively simple configurations [2]. In addition, their rotor losses are very small, which enhances their efficiency because of their nonelectric excitation [1]. The availability of high-specification materials and the improvement of power electronic converters and manufacturing technologies have further strengthened the concept of high-speed electric motors. However, the motors' high-speed operation and minimized volume have led to electrical and mechanical constraints, which have become main issues that the machine designer needs to address. These constraints affect the choice of materials used in rotors, as well as the appropriate geometry design such as the length and diameter [3].

Few academic papers discuss the design process of PM motors with speeds of up to around 150 krpm, considering the rotor vibration and the volume minimization. Gerada *et al.* [4] and Bumby *et al.* [5] discuss high-speed motors, but the power density of such motors is relatively smaller than that of PM machines because such motors are induction machines (IMs). The authors of [6]–[11] show the design process for a high-speed PM motor and its diverse applications: as a compressor, pump, machine tool, etc. In such works, however, the magnetic force distributions at the air gap and the vibration of the rotor are not considered when determining the pole–slot number combination.

This paper discusses PM machines, which have potential automotive applications, such as in the air blower cooling of fuel cells to enhance the overall performance and efficiency of the system [3], [4]. To begin with, the performance and losses of the existing surface-mounted permanent-magnet synchronous motor (SPMSM), i.e., the prototype, were analyzed through experiments to come up with plans to improve it. Based on the analysis, an improved model was designed to meet the required specifications.

This paper focuses on the essential characteristics and design methods of a motor, which should be considered when designing a high-speed motor with a maximum speed of 150 krpm. The details of these processes are discussed in the following. The first step is the consideration of vibration for ensuring mechanical stability. By determining the pole–slot number, considering vibration characteristics through the appropriate use of finite-element method (FEM) and analytical methods, the mechanical stability of the system can be ensured. The second is selecting appropriate materials and designing a magnetic circuit for minimizing iron loss. The iron loss has particularly significant effects on target performance during high-speed driving.

Manuscript received September 3, 2014; revised December 6, 2014 and January 20, 2015; accepted February 12, 2015. Date of publication March 9, 2015; date of current version November 6, 2015. This work was supported by the Ministry of Knowledge Economy, Korea, under the Convergence Information Technology Research Center support program (NIPA-2013-H0401-13-1008) supervised by the National IT Industry Promotion Agency and by the MSIP (Ministry of Science, ICT and Future Planning), Korea, under the CITRC (Convergence Information Technology Research Center) (IITP-2015-H8601-15-1005) supervised by the IITP (Institute for Information & Communications Technology Promotion). *(Corresponding author: Jung-Pyo Hong.)*

M.-S. Lim, S.-H. Chai, and J.-P. Hong are with the Department of Automotive Engineering, Hanyang University, Seoul 133-791, Korea (e-mail: hongjp@hanyang.ac.kr).

J.-S. Yang is with the Corporate Research and Development Division, Hyundai Motor Group, Hwaseong 445-706, Korea.

Color versions of one or more of the figures in this paper are available online at http://ieeexplore.ieee.org.

Digital Object Identifier 10.1109/TIE.2015.2409804

Thus, this paper examines not only the grade of a PM but also the appropriate material selection and dimension determination for minimizing iron loss to fulfill the required specifications. The final step is accurately estimating design parameters such as flux linkage, inductance, and losses by using the appropriate FEM and analytical method based on the previously established materials and shapes. The copper loss was calculated using the analytical method, considering the end coils and the operating temperature. The eddy current loss was evaluated using 3-D FEM, and the mechanical loss was determined via a no-load test of the prototype. Three-dimensional mapping of some parameters was performed, considering an armature current of 0–120 A_{rms} and a current phase angle of 0°–90°, and the results were applied for analyzing the characteristics of the motor. The iron loss, flux linkage, and inductance were calculated considering the operating points of the PM affected by the armature reaction and were mapped three-dimensionally according to the load conditions. For the 3-D FEM analysis performed in this paper, Maxwell 3-D was used, and for the 2-D FEM analysis, in-house codes were developed. The mesh size was divided into 0.2-mm elements at the air gap, thereby dividing the entire model into 17 000 elements.

As a result of the design, the power and speed of the motor were increased, and the volume was decreased by selecting appropriate materials and optimizing the core shape, stack length, number of turns per phase, etc. The validity of the design process for the proposed motor and its effectiveness were verified through load tests.

II. Analysis of Prototype and Design Specifications

The back electromotive force (BEMF) of the prototype, which an automotive company developed, at a 10 000 rpm rotational speed is approximately 1.31 V_{rms}. To analyze the losses and performance of the motor, a no-load test and a load test were conducted. In particular, the mechanical loss data of the prototype can be used to design an improved machine, and the performance of the prototype will be helpful in the formulation of the design plan.

The mechanical loss of the prototype, including its bearing and windage losses, was determined via a no-load test. This is because the mechanical loss of high-speed machines is very difficult and time consuming to evaluate exactly via analytical method and FEM. For the no-load torque test, Yokogawa WT3000 was used as the power analyzer. A dummy mass was used instead of a blower, and the air outlet in front of the dummy was closed to create a complete no-load condition. It can then be assumed that the torque was zero under the steady-state operation. Thus, the input power as the multiplication of the input current and the voltage indicated a total no-load loss because it involved mechanical loss and a no-load iron loss. In other words, the mechanical loss was calculated by subtracting the iron loss from the input power [11]. In the process, the copper loss was neglected because the square of the input current was extremely small, and the iron loss was determined via FEM. The calculated mechanical loss was finally used to design an improved model, as discussed in Section VI.

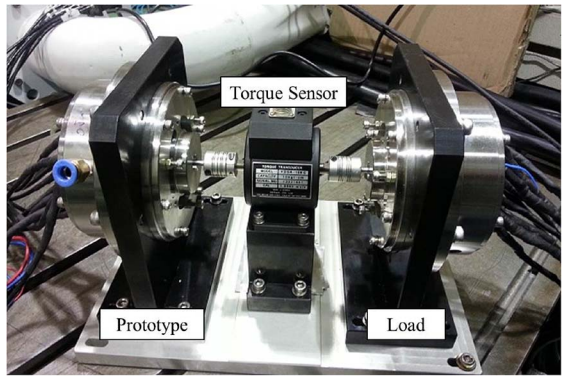

Fig. 1. Experimental setup for the load test.

TABLE I
Specifications of Prototype

Quantity	Unit	Prototype	Requirement
Supply voltage	V_{DC}	48	
Current limit	A_{rms}	120	
Power	kW	2.02	2.62
Rated torque	Nm	0.21	0.25
Rated speed	rpm	92,500	100,000
Max. speed	rpm	92,500	150,000
Outer diameter	mm	80	≤ 80
Stack length	mm	20	≤ 15

The specifications of the prototype were determined from the load test. The experiment setup for the test is shown in Fig. 1. The test was conducted by controlling the speed of the prototype and the torque of the load. The test results and the requirement specifications are shown in Table I. Given such specifications, the BEMF of the prototype was too large to reach a high speed level because the voltage was saturated at around 90 000 rpm due to the BEMF. Therefore, one of the critical design objectives is the determination of the appropriate magnitude of the BEMF to reach the rated power under 120 A_{rms} and to achieve 150 krpm under 48 V_{DC}.

In addition, to achieve a high response speed, the volume of the rotor must be reduced to minimize the moment of inertia. This is because the moment of inertia is directly related to the response speed. The rotary stability of the machine can also be improved by reducing the axial length. Thus, the design for minimizing the stack length and diameter of the rotor is critical for a high-speed machine system.

III. Pole–Slot Number Combination

The voltage and current frequencies in an inverter must be increased to make them proportional to the number of poles p so as to realize high-speed operation. However, a rising signal frequency is onerous to the inverter. The number of poles is limited by the maximum speed of the machine and by the capability of the inverter. Thus, in this paper, p was fixed at 2 to minimize the burden on the inverter. To determine the pole–slot number combination, the magnetic radial force distributions of the 2 pole–3 slot and 2 pole–6 slot motors were analyzed

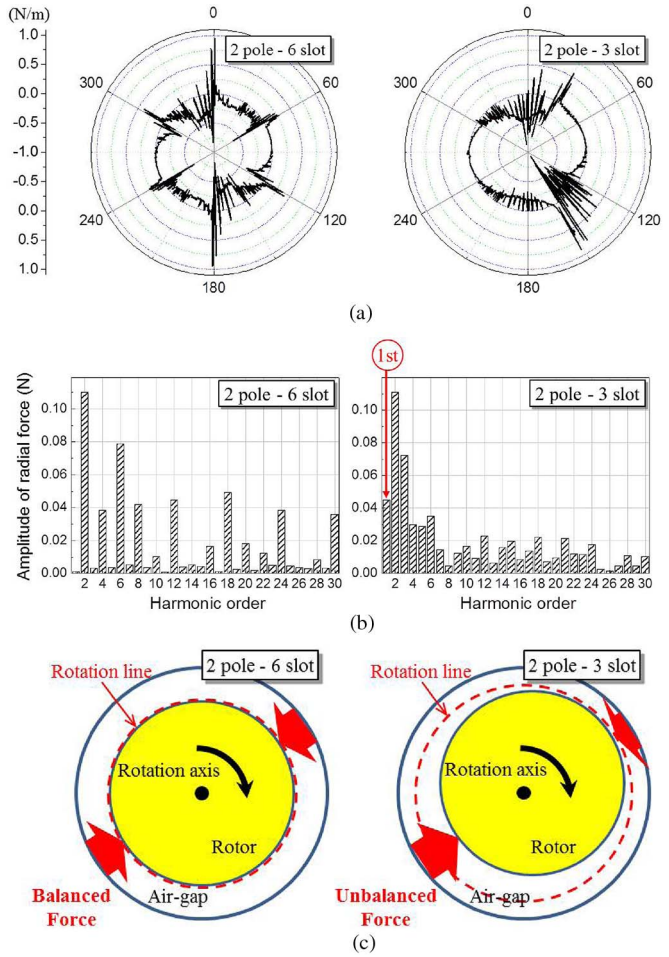

Fig. 2. Comparison of the 2 pole–3 slot and 2 pole–6 slot motors. (a) Radial force distribution. (b) Space harmonics of the radial forces. (c) Vibration of the rotor and shaft.

using the Maxwell stress tensor, as shown in (1) [12]. This is because the force distribution determines the vibration mode of the machine and affects the rotary stability [13], [14]. In (1), P_{mr} is the radial magnetic pressure, $B_{m\nu}$ and $B_{m\mu}$ are the magnetic flux densities excited by the stator harmonics ν and the rotor harmonics μ, respectively, and μ_0 is the magnetic permeability of the free space

$$P_{mr} = \frac{B_{m\nu} \cdot B_{m\mu}}{2\mu_0} \quad (\mathrm{N/m^2}). \tag{1}$$

Examples of the radial force distribution in the air gap and of the harmonic components of such forces are shown in Fig. 2(a) and (b). The rotor contributes the 2nd, 6th, 10th, etc., harmonic components because the components excited by the rotor pole are $(1 \pm 2k)N_p$ (N_p: pole number, and $k = 0, 1, 2 \ldots$). Due to the slots and the teeth, the permeance in the air gap is also periodic in space. Thus, the harmonic orders due to the slot are iN_s (N_s: slot number, and $i = 1, 2, 3, \ldots$). In addition, the difference between the harmonic components of the pole and the slot also results in the other harmonic components. In the case of the 2 pole–6 slot motor, the 4th, 6th, 8th ... harmonic components are produced because of the interaction between the flux densities of the rotor and stator in the air gap. Therefore, the 2 pole–6 slot motor has no odd harmonic component. On the other hand, the difference between the harmonic components of the pole and the slot in the 2 pole–3 slot motor can produce odd harmonic components. In particular, the 1st harmonic component is produced because the slot and the pole numbers differ by 1, which causes the unbalanced force [12]. In summary, as shown in Fig. 2(c), which shows the shaft from the axial direction, the geometrical center of the shaft deviates from the rotational center, and consequently, as the shaft rotates, a Mode 1 vibration that vibrates in the radial direction occurs. It has a major negative effect on the vibration characteristics and the rotary stability. On the other hand, the 2 pole–6 slot motor has a symmetrically balanced force distribution. Thus, the vibration level of the shaft is relatively low. Finally, the rotary stability and the vibration characteristics of the 2 pole–6 slot motor are generally much better than those of the 2 pole–3 slot motor. Therefore, the 2 pole–6 slot combination is suitable for a high-speed electric motor because it secures the stability of the system.

IV. Material Selection

At a high speed, the performance of the PM machine can be seriously limited by the iron losses [15], [16]. Thus, the iron losses under the load conditions should be minimized and considered. For the stator core, 20PNF1500 0.2-mm-ultrathin nonoriented Si–Fe electrical steel for high-frequency application was considered because it has lower iron loss than the conventional electrical steel. The iron loss of the material at 1 T and 400 Hz was about 30% lower than the loss of S08. The magnetizing flux density of the material at a 5000-A/m magnetizing force was 1.67 T.

A retaining sleeve is needed to prevent the surface-mounted PM from scattering, but an eddy current loss occurs in it. Thus, a nonmagnetic material must be used to minimize the loss, and high yield strength is required at a high temperature. As such, for the retaining sleeve, a precipitation-hardenable nickel-based alloy designed to display exceptionally high yield, tensile, and creep rupture properties at up to 704 °C temperatures was selected [17].

In SPMSM, the thickness of the PM affects the diameter of the rotor and the response speed of the machine. Therefore, a PM with high residual induction must be used to minimize its thickness. Moreover, irreversible demagnetization under a full-load condition should be avoided. As such, a Nd–Fe–B magnet with a high coercive force was used. Its residual induction was 1.22–1.26 T, its coercive force was 860–907 kA/m, its intrinsic coercive force was over 2,388 kA/m, and its maximum energy product was 287–303 kJ/m^3.

V. Geometric Design

A. Thickness of PM

The thickness of the PM was the sole geometric design parameter of the rotor because the two-pole ring-type PM was used, and the thickness of the retaining sleeve in the rotor was determined experimentally based on the rotor sleeve of the prototype. The thickness of the PM was determined analytically by considering the irreversible demagnetization. The demagnetization must be considered for high-speed

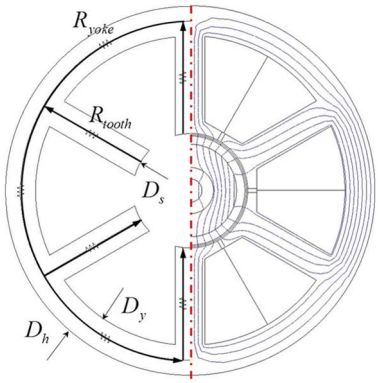

Fig. 3. Magnetic circuit and equipotential line of the simplified stator model.

machines because such machines have generally large electric loads. Equation (2) for the PM thickness l_{PM} to prevent irreversible demagnetization is shown as follows [8], [18]:

$$l_{PM} \geq \frac{m}{2} \cdot \frac{4}{\pi} \cdot \frac{\sqrt{2} \cdot I \cdot N_{ph} \cdot k_w}{p_n \cdot H_c}. \tag{2}$$

In this equation, m is the phase number, N_{ph} and p_n are the numbers of turns and pole pairs, respectively, k_w and H_c are the winding factor and the coercive force of the PM, respectively, I is the maximum rms current, and l_{PM} is 5 mm. The input maximum current in the equation is about 150% of the actual input limit current because the safety factor should be secured considering the excess current.

B. Widths of Teeth and Yoke

The widths of the teeth and the yoke in the stator were determined analytically to minimize the total magnetic resistance of the machine. Equation (3) is proposed for the calculation of the total magnetic resistance R_m of the simplified stator model. As seen from the equipotential line in Fig. 3, the flux through the tooth of the center is divided into two sides at the yoke, and the divided flux is passed along with the flux from the next tooth to the teeth on the opposite side. There are numerous fluxes with these paths flowing through the core, and an average flux path must be determined to obtain the average magnetic resistance. Therefore, assuming that the middle line of the path is the average flux path, it can be represented with the black arrows in Fig. 3. When this path is used as the circuit to find the resistance, the following (3)–(5) are obtained:

$$R_m = 2 \cdot \frac{2R_{\text{tooth}}^2 + R_{\text{tooth}}R_{\text{yoke}}}{3R_{\text{tooth}} + R_{\text{yoke}}} + R_{\text{yoke}} \tag{3}$$

where

$$R_{\text{tooth}} = \frac{D_y + D_h - 2D_s}{8\mu \cdot x \cdot L_{st}}, \quad R_{\text{yoke}} = \frac{\pi \cdot (D_y + D_h)}{\mu \cdot L_{st}(D_h - D_y)} \tag{4}$$

$$D_y = sn \cdot x \cdot \frac{2}{\pi} + \sqrt{\left(\frac{2}{\pi} \cdot sn \cdot x\right)^2 + D_s^2 - \frac{4}{\pi} \cdot sn \cdot (x \cdot D_s - AS)}. \tag{5}$$

In the preceding equation, D_h and D_s are the outer and inner diameters of the stator, respectively, D_y is the inner diameter

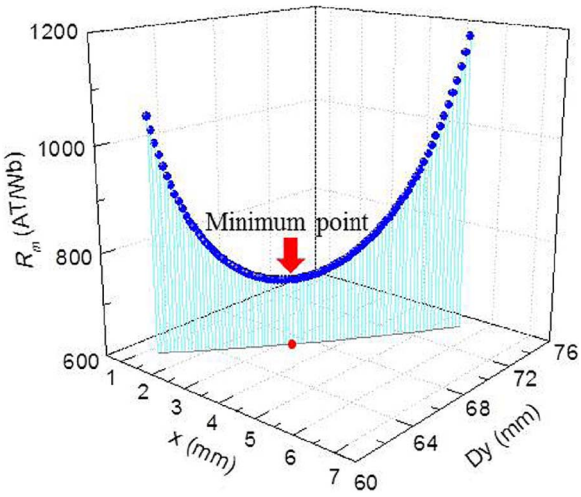

Fig. 4. Total reluctance R_m of the 2 pole–6 slot motor.

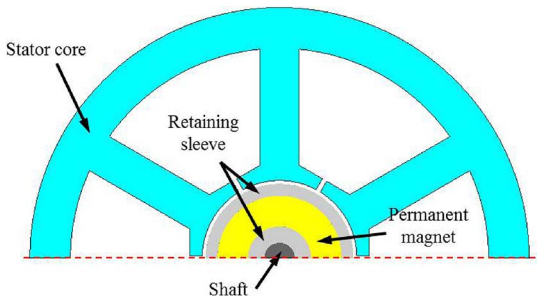

Fig. 5. Configuration of the final model of the designed motor.

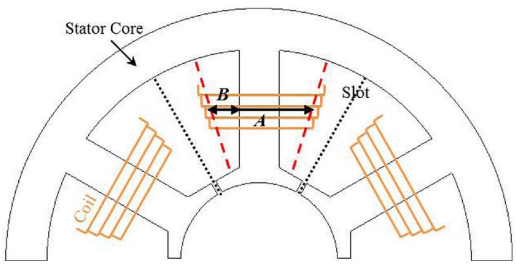

Fig. 6. Average coil span A and average height B of the end coil.

of the stator yoke, L_{stk} is the stack length of the core, sn is the number of slots, and x is half of the tooth width. D_s can be determined based on the rotor diameter and length of the air gap, and D_y is calculated using (5), considering the slot area AS determined from the current density and the number of turns. The calculated magnetic resistance that varied with the x and D_y of the 2 pole–6 slot motor is shown in Fig. 4. Finally, x and D_y should be determined by finding the minimum point of the total reluctance R_m of the motor. Fig. 5 shows the resulting configuration of the designed motor.

VI. Loss Evaluation

A. Copper Loss

In high-speed machines, the skin effect occurs in the wire due to the high-frequency ac current. Thus, the wire should be thin enough to avoid the skin effect. In other words, the diameter of

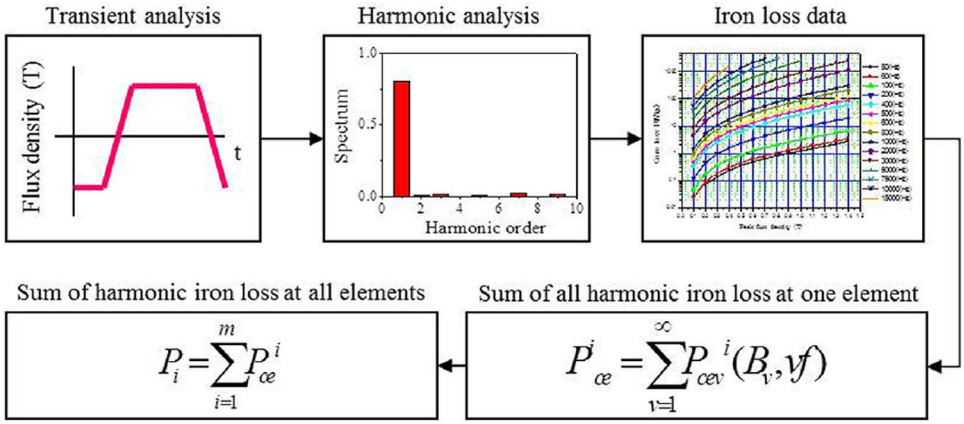

Fig. 7. Iron loss calculation process.

the copper wire should be smaller than the skin depth. Equation (6) for the skin depth is

$$\delta = \sqrt{\frac{1}{\pi f \mu_0 \mu_r \sigma}} \tag{6}$$

where δ and f are the skin depth and the frequency, respectively [19], μ_0 and μ_r are the permeability of the free space and the relative magnetic permeability of the conductor, respectively, and σ is the conductivity of the conductor. At the maximum speed, f is 2.5 kHz, and the conductivity of copper is 5.80×10^7 $1/\text{ohm} \cdot \text{m}$.

The diameter of the wire was determined, and the copper loss was calculated analytically, considering the end coils. It was assumed that the slot was uniformly filled with coils. In the model with a concentrated winding, A was the average coil span, and B was the assumed average height of the end coils, as shown in Fig. 6. Thus, (7) for calculating the phase resistance R_a is

$$R_a = \rho_c \cdot \frac{2 \cdot (L_{stk} + A + 2B) \cdot N_{ph}}{\pi \cdot r^2} \cdot [1 + \alpha \cdot (T - 20^\circ\text{C})] \tag{7}$$

where L_{stk} and N_{ph} are the stack length and the number of turns in series per phase, respectively, r is the radius of the coil, T is the operating temperature in degrees Celsius, ρ_c is the resistivity of copper at 20 °C, and α is the temperature coefficient of the resistivity.

B. Iron Loss and Eddy Current Loss

Fig. 7 shows the process of determining the iron losses. Depending on the magnitude and phase of the noise, the operating point of the PM is renewed, and considering the harmonics of the flux density, the iron loss is calculated. Here, the magnitude and phase of up to the 30th harmonics were considered.

The aforementioned process is described in detail as follows [20], [21].

Step 1) Using nonlinear FEM, the flux density at each mesh for one electrical angle period is calculated, as the rotor is rotated under a load condition. Here, the flux density is calculated as the normal and tangential components.

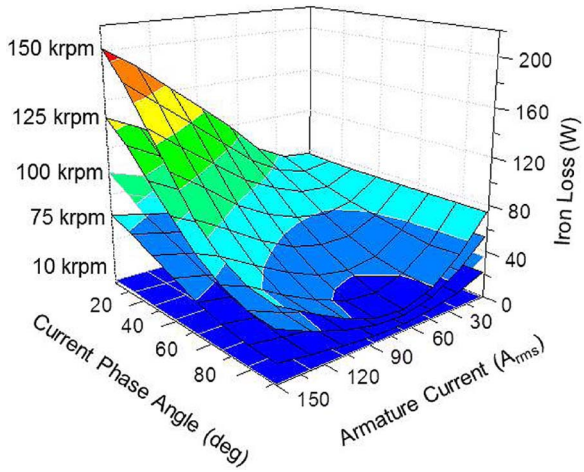

Fig. 8. Iron loss according to the armature currents and current phase angles.

Step 2) Using the flux density from Step 1), Fourier transform is performed to find the magnitude and the phase of the fundamental and harmonic components.

Step 3) From the iron loss data for the material, the iron loss corresponding to the frequency and the flux density of each harmonic is calculated considering its phase. The material information is based on the empirical data.

Step 4) The sum of the iron losses due to the harmonic components at each mesh is calculated.

Step 5) The iron losses of all the meshes are added to determine the total iron loss of the machine.

As a result of the aforementioned process, the iron loss 3-D map of the motor according to various armature currents of 0–150 A_{rms} and current phase angles of 0°–90° was obtained, as shown in Fig. 8. The map shows that the iron loss increases in a high-speed region when the current phase angle β is 0°. This aspect differed, however, when β was close to 90°.

In addition, the total eddy current loss in the PM and the retaining sleeve is critical in high-speed machines. This is because the eddy current loss is proportional to the square of the frequency [22], [23]. Thus, in this paper, the eddy current loss in the PM and the retaining sleeve was considered using Maxwell

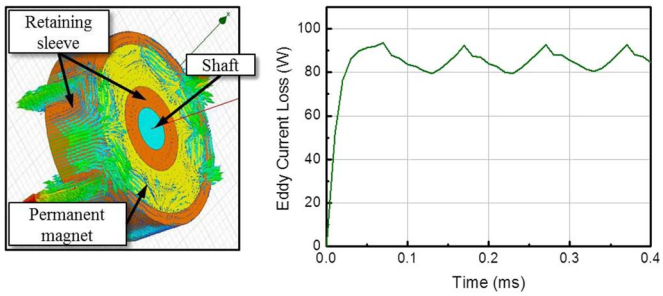

Fig. 9. Eddy current analysis of the designed model. (a) Eddy current in the rotor. (b) FEM result (transient analysis).

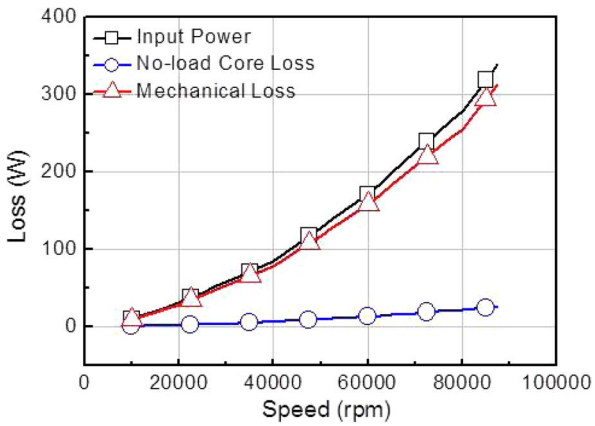

Fig. 10. No-load test results.

3-D. Fig. 9(a) and (b) shows the vector flow and the total loss of the eddy current in the rotor, respectively. Three-dimensional transient analysis was conducted with the half-model of the rotor, and it was symmetric with respect to the axial plane. The results of the FEM show that the average iron and eddy current losses were determined to be about 93.59 and 85.32 W under the rated-speed full-load condition.

C. Mechanical Loss

The shaft and bearing system of the improved motor was the same as that of the prototype. Therefore, the mechanical loss obtained from the no-load test of the prototype, as described in Section II, can be used to design the improved machine as it is. This is because it can be assumed that the mechanical loss of the high-speed machine consists mainly of the bearing and windage losses. The test was conducted at around 90 000 rpm because of the performance limitation of the prototype, as shown in Fig. 10. Therefore, to estimate the mechanical loss over the maximum speed of the prototype, the quadratic function of the speed was interpolated as

$$P_{\text{mech}} = c_1 + c_2 \cdot n + c_3 \cdot n^2 \quad \text{(W)}$$
$$\begin{pmatrix} c_1 = 3.789 & \text{(W)} \\ c_2 = 9.151 \times 10^{-4} & \text{(W/rpm)} \\ c_3 = 5.078 \times 10^{-8} & \text{(W/rpm}^2\text{)}. \end{pmatrix} \quad (8)$$

In the preceding equation, P_{mech} is the mechanical loss in watts, and n is the rotor speed in revolutions per minute. In this equation, n cannot be zero, or P_{mech} will also be zero.

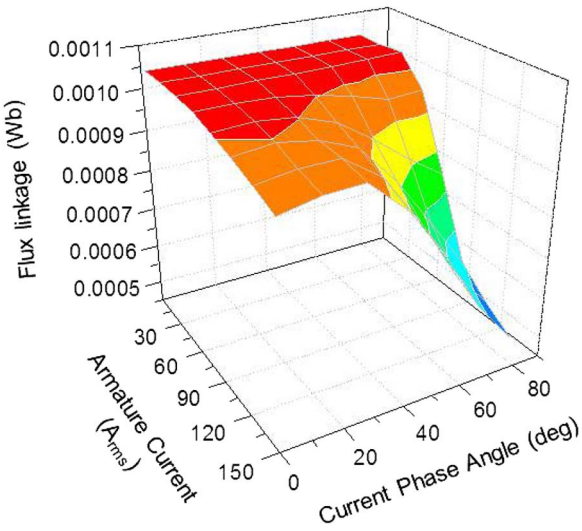

Fig. 11. Flux linkage ψ_e according to the armature currents and current phase angles.

VII. Design Results and Verification

A. Characteristics of Designed Motor

In this paper, the equivalent circuit method considering the iron loss was used to predict the machine performance under a steady-state condition [23]. Thus, the voltage and torque equations based on the equivalent circuit were used. The voltage equations are shown in (9) and (10), and the output torque is expressed as (11). i_d and i_q are the d- and q-axis armature currents, v_d and v_q are the d- and q-axis voltages, i_{od} and i_{oq} are the currents subtracted from the d- and q-axis currents resulting in the iron losses from the input currents i_d and i_q, respectively, R_a is the phase resistance of the armature winding, R_c is the equivalent resistance of the iron loss; L_d and L_q are the d- and q-axis inductances, p is the differential operator as d/dt, ψ_e is the rms flux linkage of the PM, p_p is the number of pole pairs, and ω and ω_m are the electrical and mechanical speeds in radians per second

$$\begin{bmatrix} cv_d \\ v_q \end{bmatrix} = R_a \begin{bmatrix} ci_{od} \\ i_{oq} \end{bmatrix} + \left(1 + \frac{R_a}{R_c}\right) \begin{bmatrix} cv_{od} \\ v_{oq} \end{bmatrix} + p \begin{bmatrix} ccL_d & 0 \\ 0 & L_q \end{bmatrix} \begin{bmatrix} ci_{od} \\ i_{oq} \end{bmatrix} \quad (9)$$

$$\begin{bmatrix} cv_{od} \\ v_{oq} \end{bmatrix} = \begin{bmatrix} cc0 & -\omega L_q \\ \omega L_d & 0 \end{bmatrix} \begin{bmatrix} ci_{od} \\ i_{oq} \end{bmatrix} + \begin{bmatrix} c0 \\ \sqrt{3}\omega\psi_e \end{bmatrix} \quad (10)$$

$$T = p_p \left[\sqrt{3}\psi_e i_{oq} + (L_d - L_q) i_{od} i_{oq}\right] - \left(\frac{P_{\text{mech}}}{\omega_m}\right). \quad (11)$$

The BEMF and the cogging torque were obtained from the nonlinear FEM. The BEMF at 10 000 rpm under the no-load condition was 1.092 V_{rms}, and the cogging torque (peak to peak) was 0.18 mNm. The d- and q-axis inductances L_d and L_q are defined as the magnitudes of the flux linkage per unit current. In this paper, the operating point of the PM was calculated considering all load conditions, and the flux linkage ψ_e and the inductances were estimated through a nonlinear FEM that accounted for the calculated result. The results are shown in Figs. 11 and 12. The flux linkage and the inductances decreased

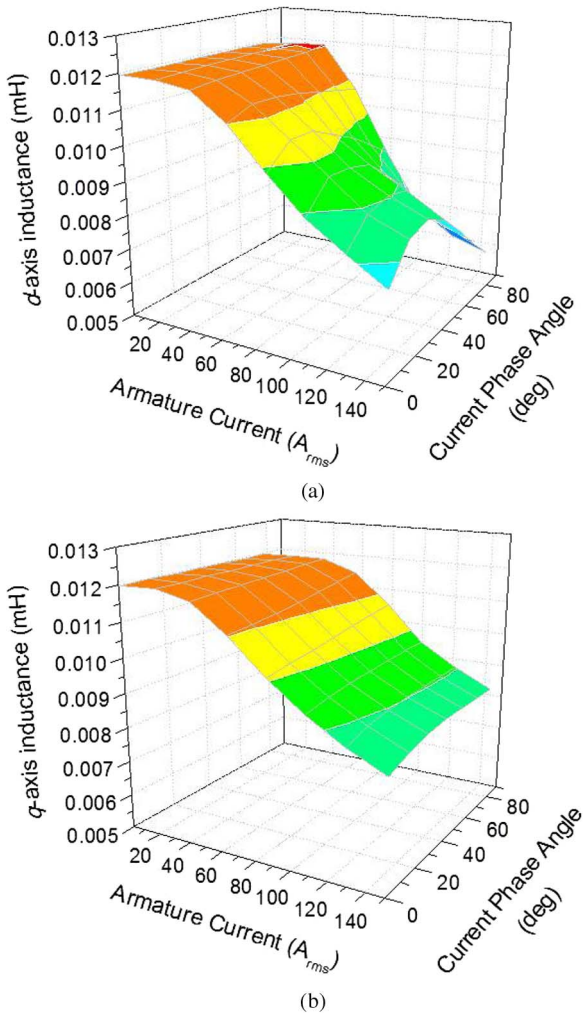

Fig. 12. d- and q-axis inductances according to the armature currents and current phase angles. (a) d-axis inductance. (b) q-axis inductance.

when the armature current increased due to the saturation of the core. Furthermore, the flux linkage rapidly decreased when the current phase angle was close to 90°, i.e., flux weakening. Under the no-load or low-load condition, the d- and q-axis inductances were similar. However, under the high-load conditions, there was a discrepancy between the d- and q-axis inductances even though it was an SPMSM, which was originally a nonsalient pole machine. Therefore, the flux linkage and the inductance maps according to the load conditions were used to predict the performance of the designed motor.

The proportion of the losses at the rated and maximum speed is shown in Fig. 13. The iron loss was much lower than the mechanical loss since the core material was selected appropriately. Furthermore, the electrical frequency was not very high because the machine has only two poles. After all the previously described losses were considered, the efficiency was found to have been 71.6% at the rated speed of 100 krpm and 63.4% at the maximum speed of 150 krpm.

The output torque T was calculated using the i_{od} and i_{oq} values obtained using (8) and (9), meeting the d- and q-axis voltage and current limit requirements of the machine. In addition, the mechanical loss per rotor speed was subtracted from the electric torque to find the exact output torque, as shown in (10).

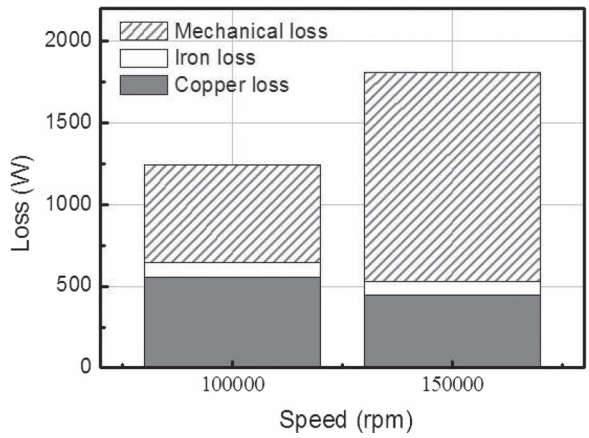

Fig. 13. Copper, iron, and mechanical loss proportions in the designed motor.

B. Design Verifications

The magnetic flux density distribution of the core is shown in Fig. 14. Under the no-load condition, the average flux densities at the stator teeth and yoke were similar as 0.96–0.97 T due to the stator geometric design described in Section V. Under the full-load condition, the flux density distribution was rotated on the q-axis because of the q-axis input current. Due to the armature reaction, the average flux density at the teeth and yoke near the q-axis rose to 1.51–1.54 T. The simulation results conclusively show that the magnitude of the flux density in the stator teeth and yoke was well balanced.

To verify the validity of the design process, the designed model was set up, and an experiment was conducted. The specifications of the designed motor that fulfilled the requirements are shown in Table II. The BEMF under the no-load condition was tested at 33 619.8 rpm, as shown in Fig. 15. The error between the test result of 3.63 V_{rms} and the FEM result of 3.67 V_{rms} was 1.11%. The torque and power test results were compared with those in the simulation, as shown in Fig. 16. The motor was driven via Id = 0 control. The power reached 2.62 kW at the rated speed. Over the base speed, the reference torque was purposely linearly decreased with the q-axis current, as was the output power after the base speed. Fig. 17 shows the d- and q-axis input currents according to the motor speed. The d-axis current was consistently zero, and the q-axis current was linearly reduced from the base speed, such as the torque. Due to the reduced q-axis current, the voltage drop caused by the phase resistance and inductance were decreased. Thus, the machine could be operated over the base speed. As the design result, the volume of the designed model decreased, and the rated power and the maximum speed increased, as shown in Fig. 18.

The speed characteristics of the designed motor according to the drive conditions are compared in Fig. 19, and the drive conditions of the motor are shown in Table III. Over the rated speed, the torque and power were decreased. Thus, the speed characteristics were analyzed at the rated speed. As a result, the motor speed under Mode 1 increased faster due to the higher torque than that under Modes 2 and 3. The time that it took to reach 100 krpm under Drive Mode 1 was about 22.50% and 40.12% faster than under Modes 2 and 3, respectively. It was

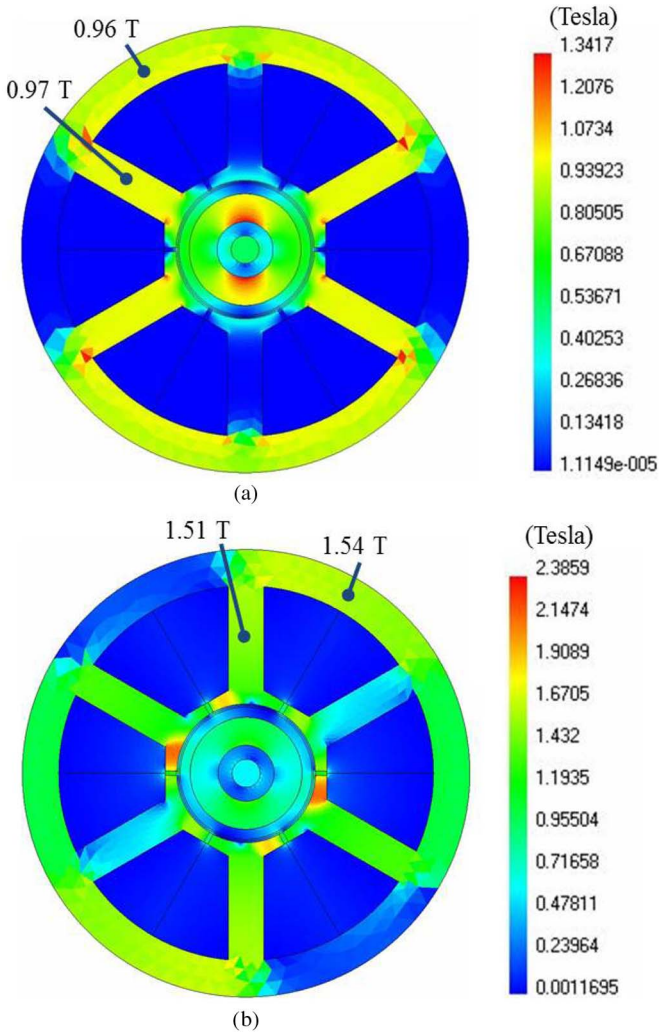

Fig. 14. Magnetic flux density distribution of the core at the stator teeth and yoke. (a) Flux density under the no-load condition. (b) Flux density under the full-load condition.

TABLE II
SPECIFICATIONS OF DESIGNED MOTOR

Quantity	Unit	Value
Supply voltage	V_{DC}	48
Current limit	A_{rms}	120
Power	kW	2.62
Torque	Nm	0.25
Rated speed	rpm	100,000
Max. speed	rpm	150,000
Outer diameter	mm	80
Stack length	mm	13
Pole-slot number	-	2pole- 6slot
Core material	-	20PNF1500
Magnet material	-	Nd-Fe-B
Sleeve material	-	Precipitation-hardenable nickel-based alloy

verified that a higher motor torque and power quickly increase the motor speed, which means that the performance of the air blower can be improved.

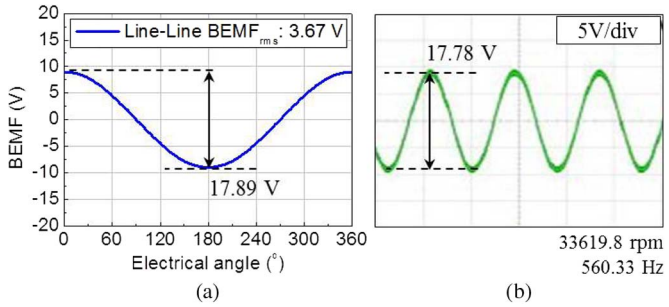

Fig. 15. BEMF at 33 619.8 rpm under the no-load condition. (a) FEM result. (b) Experiment result.

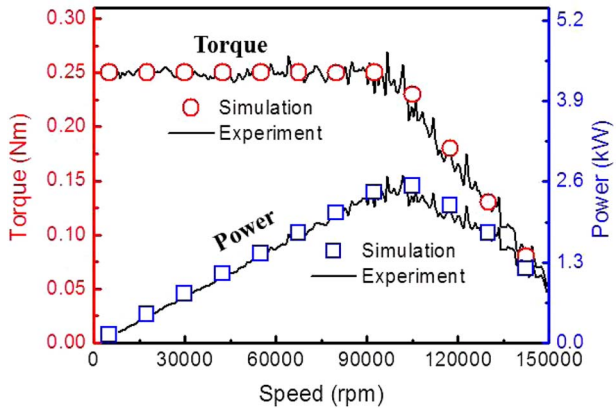

Fig. 16. Performance of the designed model.

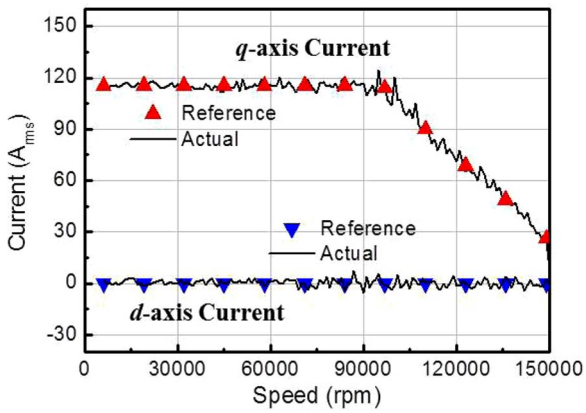

Fig. 17. Reference and actual d- and q-axis input currents.

In conclusion, in this paper, the validity of the proposed design method and the performance of the proposed SPMSM were verified through an experiment. Furthermore, the performance of the air blow system was improved using the proposed motor.

VIII. CONCLUSION

In this paper, the design process for the 2.62-kW 150-krpm high-speed SPMSM was proposed. The process of determining the pole–slot number and the material selection method was described to minimize the vibration and the losses. As the results, 2 pole–6 slot was selected. In the case of the material, ultrathin nonoriented Si–Fe electrical steel for high-frequency

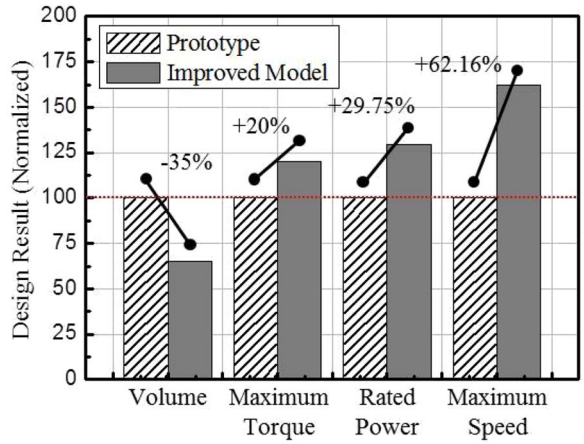

Fig. 18. Comparison of the prototype and the designed model.

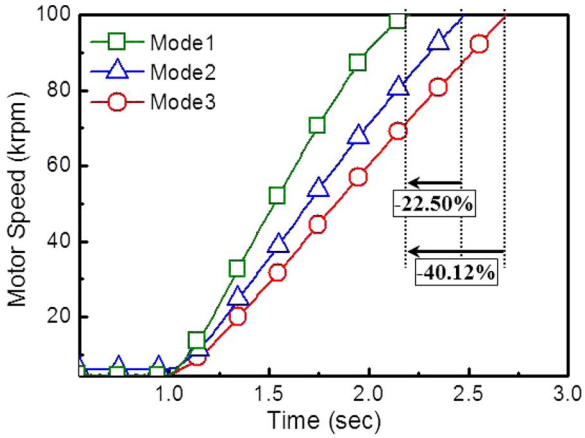

Fig. 19. Speed characteristics of the designed motor as the test results according to the operation mode.

TABLE III
DRIVE MODES OF MOTOR

Drive conditions	Motor torque until the rated speed
Mode 1	Full torque
Mode 2	50 % torque
Mode 3	33 % torque

application was used as the core material. A precipitation-hardenable nickel-based alloy was used as the sleeve material, and a Nd–Fe–B magnet was used. In addition, not only the geometric design process parameters such as the widths of the core and the thickness of the PM but also the mechanical, copper, and iron loss evaluation method were discussed, based on the FEM, experimental, and analytical approaches. Thus, the saturation level at the teeth and yoke was well balanced, and a motor that would fulfill the requirement specifications was designed. With this proposed method, the volume of the motor was reduced by about 35%, and the maximum torque was increased by about 20%. The rated power and the maximum speed were increased by about 29.75% and 62.16%, respectively, through the appropriate design and control. Finally, the effectiveness of the motor was verified through an experiment.

REFERENCES

[1] A. Binder, T. Schneider, and M. Klohr, "Fixation of buried and surface mounted magnets in high-speed permanent magnet synchronous motors," in *Conf. Rec. IEEE IAS Annu. Meeting*, Oct. 2005, vol. 4, pp. 2843–2848.

[2] A. Borisavljevic, H. Polinder, and J. A. Ferreira, "On the speed limits of permanent-magnet machines," *IEEE Trans. Ind. Electron.*, vol. 57, no. 1, pp. 220–227, Jan. 2010.

[3] D. K. Hong, B. C. Woo, J. Y. Lee, and D. H. Koo, "Ultra high speed motor supported by air foil bearings for air blower cooling fuel cells," *IEEE Trans. Magn.*, vol. 48, no. 2, pp. 871–874, Feb. 2012.

[4] D. Gerada, A. Mebarki, N. L. Brown, K. J. Bradley, and C. Gerada, "Design aspects of high-speed high-power laminated-rotor induction machines," *IEEE Trans. Ind. Electron.*, vol. 58, no. 9, pp. 4039–4047, Sep. 2011.

[5] J. R. Bumby, E. Spooner, and M. Jagiela, "Equivalent circuit analysis of solid-rotor induction machines with reference to turbocharger accelerator applications," *Proc. Inst. Elect. Eng. Elect. Power Appl.*, vol. 153, no. 1, pp. 31–39, Jan. 2006.

[6] C. C. Hwang, S. S. Hung, C. T. Liu, and S. P. Cheng, "Optimal design of a high speed SPM motor for machine tool applications," *IEEE Trans. Magn.*, vol. 50, no. 1, Jan. 2014, Art. ID. 4002304.

[7] S. M. Jang, H. W. Cho, and S. K. Choi, "Design and analysis of a high-speed brushless dc motor for centrifugal compressor," *IEEE Trans. Magn.*, vol. 43, no. 6, pp. 2573–2575, Jun. 2007.

[8] N. Bianchi, S. Bolognani, and F. Luise, "Analysis and design of a PM brushless motor for high-speed operations," *IEEE Trans. Energy Convers.*, vol. 20, no. 3, pp. 629–637, Sep. 2005.

[9] M. Sridharbabu, T. Kosaka, and N. Matsui, "Design analysis and improvement high speed hybrid excitation motor for main spindle drive in machine tools based on experimental results of prototype machine," in *Proc. IEEE 8th ICPE ECCE Asia*, May/Jun. 2011, pp. 1935–1939.

[10] T. Schneider and A. Binder, "Design and evaluation of a 60 000 rpm permanent magnet bearingless high speed motor," in *Proc. IEEE 7th Int. Conf. PEDS*, Nov. 2007, pp. 1–8.

[11] P.-D. Pfister and Y. Perriard, "Very-high-speed slotless permanent-magnet motors: Analytical modeling, optimization, design, and torque measurement methods," *IEEE Trans. Ind. Electron.*, vol. 57, no. 1, pp. 296–303, Jan. 2010.

[12] T. Sun, J. M. Kim, G. H. Lee, J. P. Hong, and M. R. Choi, "Effect of pole and slot combination on noise and vibration in permanent magnet synchronous motor," *IEEE Trans. Magn.*, vol. 47, no. 5, pp. 1038–1041, May 2011.

[13] J. Boisson, F. Louf, J. Ojeda, X. Mininger, and M. Gabsi, "Analytic approach for mechanical resonance frequencies of high-speed machines," *IEEE Trans. Ind. Electron.*, vol. 61, no. 6, pp. 3081–3088, Jun. 2014

[14] H. Y. Yang, Y. C. Lim, and H. C. Kim, "Acoustic noise/vibration reduction of a single-phase SRM using skewed stator and rotor," *IEEE Trans. Ind. Electron.*, vol. 60, no. 10, pp. 4292–4300, Oct. 2013

[15] G. Pellegrino, P. Guglielmi, A. Vagati, and F. Villata, "Core losses and torque ripple in IPM machines: Dedicated modeling and design tradeoff," *IEEE Trans. Ind. Appl.*, vol. 46, no. 6, pp. 2381–2391, Nov./Dec. 2010.

[16] M. Dems, and K. Komeza, "Performance characteristics of a high-speed energy-saving induction motor with an amorphous stator core," *IEEE Trans. Ind. Electron.*, vol. 61, no. 6, pp. 3046–3055, Jun. 2014

[17] E. C. Lovelace, T. M. Jahns, T. A. Keim, and J. H. Lang, "Mechanical design considerations for conventionally laminated, high-speed, interior PM synchronous machine rotors," *IEEE Trans. Ind. Appl.*, vol. 40, no. 3, pp. 806–812, May/Jun. 2004.

[18] J. W. Jung, S. H. Lee, and J. P. Hong, "Optimum design for eddy current reduction in permanent magnet to prevent irreversible demagnetization," in *Proc. IEEE ICEMS*, Oct. 2007, pp. 949–954.

[19] H. M. Hamalainen, J. J. Pyrhonen, and J. Puranen, "Minimizing skin effect in random wound high speed machine stator," in *Proc. IEEE EUROCON*, May 2009, pp. 752–757.

[20] B. H. Lee *et al.*, "Modeling of core loss resistance for d-q equivalent circuit analysis of IPMSM considering harmonic linkage flux," *IEEE Trans. Magn.*, vol. 47, no. 5, pp. 1066–1069, May 2011.

[21] G. H. Kang, J. P. Hong, G. T. Kim, and J. W. Park, "Improved parameter modeling of interior permanent magnet synchronous motor based on finite element analysis," *IEEE Trans. Magn.*, vol. 36, no. 4, pp. 1867–1870, Jul. 2000.

[22] N. Zhao, Z. Q. Zhu, and W. Liu, "Comparison of rotor eddy current losses in permanent magnet motor and generator," in *Proc. IEEE ICEMS*, Aug. 2011, pp. 1–6.

[23] J. Hur, "Characteristic analysis of interior permanent-magnet synchronous motor in electrohydraulic power steering systems," *IEEE Trans. Ind. Electron.*, Vol. 55, no. 6, pp. 2316–2323, Jun. 2008.

Myung-Seop Lim received the Bachelor's degree in mechanical engineering and the Master's degree in automotive engineering from Hanyang University, Seoul, Korea, in 2012 and 2014, respectively, where he is currently working toward the Ph.D. degree in automotive engineering.

His research interests are electric machine design for automotive and robot applications, and sensorless drive.

Seung-Hee Chai received the degree in mechanical engineering from Hanyang University, Seoul, Korea, in 2009, where he is currently working toward the Ph.D. degree in automotive engineering.

His main fields of interests are the optimization, analysis, design of electric machines for vehicle traction and the numerical analysis of electromagnetics.

Jae-Sik Yang received the Bachelor's degree in mechanical engineering and the Master's degree in mechanical engineering from the Korea Advanced Institute of Science and Technology, Korea, in 2005 and 2007, respectively.

He currently works as a Senior Research Engineer at the Hyundai Motor R&D Center, Hwaseong, Korea. His research interests are electric machine design for automotive and sensorless drive.

Jung-Pyo Hong (SM'97) received the Ph.D. degree in electrical engineering from Hanyang University, Seoul, Korea, in 1995.

From 1996 to 2006, he was a Professor with Changwon National University, Chang-won, Korea. Since 2006, he has been working as a Professor in Hanyang University. His research interests are the design of electric machines and the optimization and numerical analysis of electromechanics.